Investigating the Transition from Elevated Multicellular Convection to Surface-Based Supercells as Observed in the Indiana and Ohio Tornado Outbreak of 24 August 2016 using a WRF Model Simulation and Perturbation Pressure Decomposition

KEVIN GRAY*AND JEFFREY FRAME

Department of Atmospheric Sciences, University of Illinois at Urbana-Champaign, Urbana, IL

1. Introduction and motivation

On 24 August 2016, a tornado outbreak with 24 confirmed tornadoes impacted Indiana and Ohio, six of which were significant (rated EF-2 or greater on the Enhanced Fujita Scale). This event was unusual as it caught many meteorologists by surprise. For example, the Storm Prediction Center (SPC) 1300 UTC Day 1 Tornado Risk area did not include Indiana or Ohio (Fig. 1). Morning convection-allowing model output also did not depict significant updraft helicity streaks (> 100 m^2 s^{-2}; Clark et al. 2013) over this area. This forecast was complicated by antecedent convection, a mesoscale convective vortex (MCV), and surface boundaries.

Convection near the Nebraska/Iowa border the night prior to the outbreak produced an MCV that progressed eastward through Iowa and then across northern Illinois and Indiana during the day on 24 August 2016. This convection also generated an outflow boundary that was tracked through Iowa during the early morning hours. Convection formed ahead of this boundary and eventually organized into a linear cluster in northern Illinois. Another linear cluster developed along the outflow boundary as it entered northwestern Illinois, such that there were two clusters of elevated convection over Illinois that morning (Fig. 2). As the leading cluster entered Indiana, it weakened and dissipated. Anvil shading from this cluster resulted in a differential heating boundary identifiable on visible satellite imagery and in surface observations (Fig. 3). As the trailing cluster entered Indiana, the differential heating boundary moved northeastward. The trailing cluster then transitioned from disorganized elevated convection into three discrete supercells, all of which were tornadic. The supercells began to form just after 1800 UTC and the formation of each coincided with the northward progression of the differential heating boundary. A thorough mesoscale analysis of satellite, surface, and radar observations from this outbreak is presented in a companion study (Frame and Gray 2018).

Many previous studies have focused on how storms

transition from surface based to elevated (e.g., Parker 2008; Geerts et al. 2017) and several studies have been conducted on how supercells grow upscale into multicellular complexes (e.g., Bluestein and Weisman 2000; Finley et al. 2001). A case study of this event fits into a relatively unexplored area in the literature, investigating the transition from elevated to surface-based convection. It is also fairly uncommon to see lines of storms split into discrete supercells. We were able to find only one study in which this was the case (Burgess and Curran 1985). Their study attributed the development of supercells from a line of storms to a low-level jet that increased low-level shear and reestablished a capping inversion. Owing to the the inversion, only rotating elements within the linear convection persisted, likely because of their associated upward-directed perturbation pressure gradient forces (e.g., Rotunno and Klemp 1982).

We investigated this transition using a high-resolution Weather Research and Forecasting (WRF) model simulation. The model configuration is described in section 2. Section 3 presents an analysis of the WRF simulation including an overview, vertical cross sections, and trajectory, vorticity budget, and perturbation pressure decomposition analyses. Conclusions are discussed in section 4.

2. WRF model configuration

The event was simulated using the WRF model, version 3.8.1 (Skamarock et al. 2008). The outer domain measures $1695 \times 1695 \times 20$ km with 60 vertical levels. The horizontal resolution of the outer domain is 3 km, the vertical resolution is stretched from 50 m to 250 m below 2 km and is 377.5 m above 2 km, and the timestep is 3 seconds. An inner domain with dimensions of $682 \times 682 \times 20$ km and 60 vertical levels is centered over Illinois and Indiana with 1 km horizontal resolution, the same vertical resolution as the outer domain, and a timestep of 1 second (Fig. 4). Both domains utilize open boundary conditions. The model was initialized with the 12-km resolution 0600 UTC 24 August 2016 North American Mesoscale (NAM) model analysis. Data were provided for the lateral boundary condi-

---
Corresponding author address: Kevin Gray, Department of Atmospheric Sciences, University of Illinois at Urbana-Champaign, 1301 W. Green St., Urbana, IL, 61801; *e-mail*: kevintg2@illinois.edu
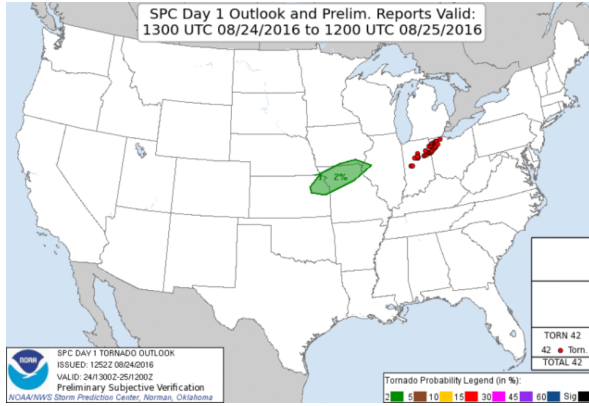
FIG. 1. SPC probability of a tornado within 25 miles of a point (green area) from the Day 1 Convective Outlook issued at 1300 UTC. Red dots are preliminary tornado reports.
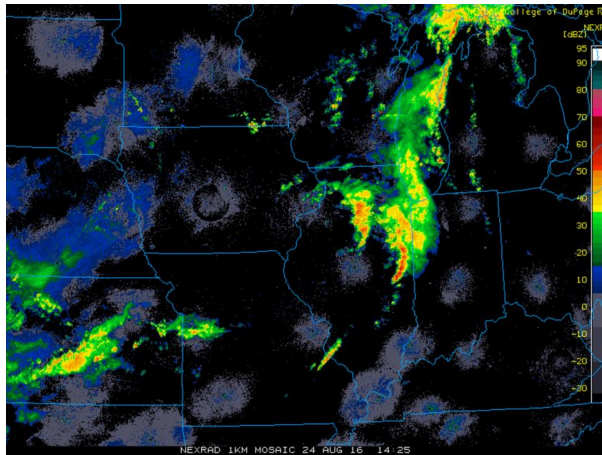

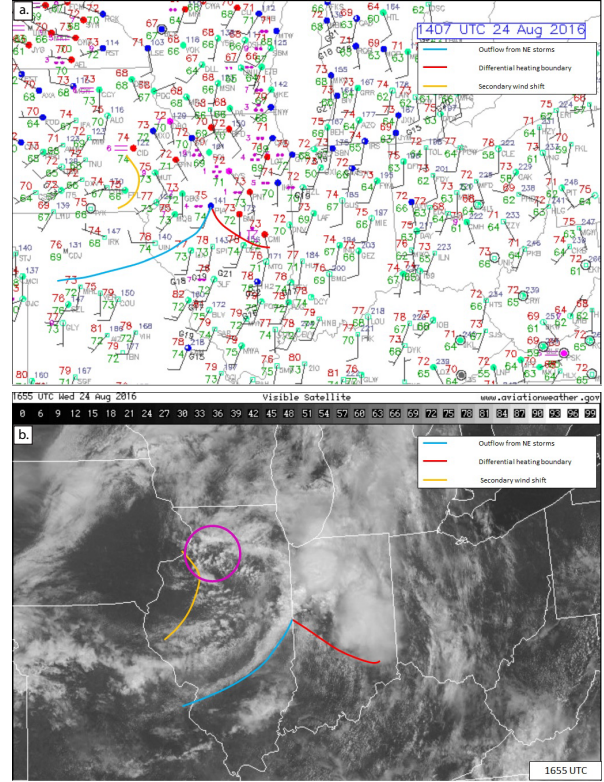FIG. 2. Radar reflectivity (dBz) mosaic at 1425 UTC.

FIG. 3. (a) Surface observations at 1407 UTC. The blue line is the outflow boundary from the evening storms, the red line is the differential heating boundary, and the orange line is a secondary wind shift. (b) Visible satellite imagery at 1655 UTC. Colored lines are as in (a) and the pink circle indicates the MCV location.

tions of the outer domain every six hours from the 1200 and 1800 UTC 24 August NAM analyses, and the 0000 UTC 25 August NAM analysis. The inner domain was initialized at 1400 UTC and the simulation terminated at 0000 UTC. The Milbrandt-Yau two-moment cloud microphysics parameterization was utilized on both domains (Milbrandt and Yau 2005). The Rapid Radiative Transfer Model for General Circulation Models was employed for both longwave and shortwave radiation (Mlawer et al. 1997; Iacono et al. 2000). The Revised MM5 Monin-Obukhov surface-layer scheme (Jiménez et al. 2012) and the Unified Noah land-surface model were used (Livneh et al. 2011). The MYNN 2.5 level TKE scheme was utilized for the boundary layer (Nakanishi

and Niino 2006) along with the 2D Smagorinsky first-order turbulence closure model (Xue et al. 2000). There was no convective parameterization employed on either domain.

3. WRF simulation analysis

a. Simulation overview

The WRF simulation accurately captures many details of the outbreak, including the location of the MCV, the differential heating boundary (co-located with the edge of the anvil)[1], and the transition of unorganized elevated convection to a surface-based supercell (Fig. 5). A time series of maximum 1 km relative vertical vorticity (ζ) and the mean 4 km vertical velocity (w) within a 5×5 km box centered on the maximum 1 km ζ elucidate intensity changes within the simulated storm (Fig. 6). The

[1]The 0.1 kg m^{-2} contour of total column integrated ice is used as a proxy for the extent of the anvil.
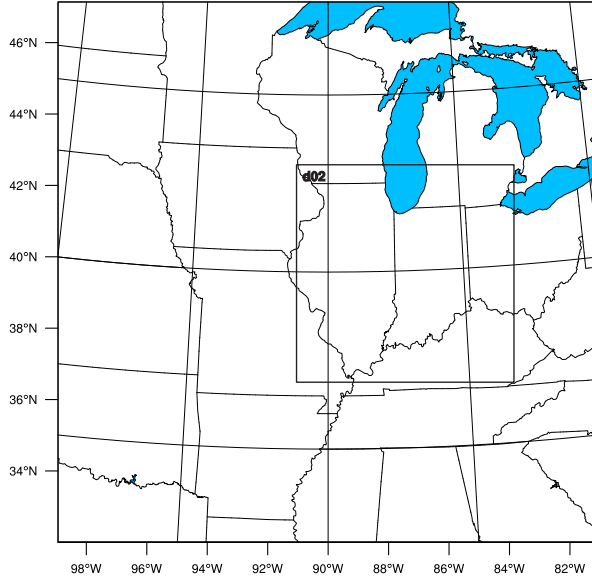
FIG. 4. Domains used in the WRF simulation.

FIG. 5. Simulated 1 km reflectivity (dBz; shaded), surface temperature (°C; red contours), total column integrated ice of 0.1 kg m^{-2} (black contour), and surface winds (kts; barbs) at (a) 1530 and (b) 1600 UTC. The blue lines are the locations of the vertical cross sections in Fig. 7.

updrafts are elevated through roughly 1530 UTC, as indicated by trajectory analyses in the next section. During this time, mean 4 km w is around 6 m s^{-1} and 1 km ζ has a brief peak at 0.02 s^{-1} associated with a shallow vortex along a gust front. The storms then become surface-based between 1540-1600 UTC. After this transition, the mean 4 km w steadily increases, with a peak around 16 m s^{-1} at 1650 UTC, followed by a peak in 1 km ζ of 0.032 s^{-1} at 1700 UTC. The supercell then weakens as the mesocyclone cycles. After the storm recycles, the supercell reaches its maximum intensity from roughly 1815-1900 UTC, and then it becomes outflow dominant and weakens thereafter.

b. Vertical cross sections

The blue vertical lines in Figs. 5a,b indicate the locations of vertical cross sections displayed in Figs. 7a,b. Vertical cross sections before 1530 UTC indicate that convection is elevated and multicellular (not shown). The vertical cross section at 1530 UTC exhibits elevated updrafts, with little vertical velocity below 1 km (Fig. 7a). Some ζ develops around 1 km as a weak updraft of 4-6 m s^{-1} at this level tilts horizontal vorticity generated by strong vertical wind shear in the 0-1 km layer (Fig. 7c). The 1600 UTC cross section exhibits a surface-based updraft, with w around 16 m s^{-1} below 1 km and extending upward to 8 km. Co-located with this updraft is ζ greater than 0.015 s^{-1}. This analysis suggests the transition from elevated to surface-based convection occurs between 1530 and 1600 UTC. Cross sections at later times (not shown) indicate that the storm
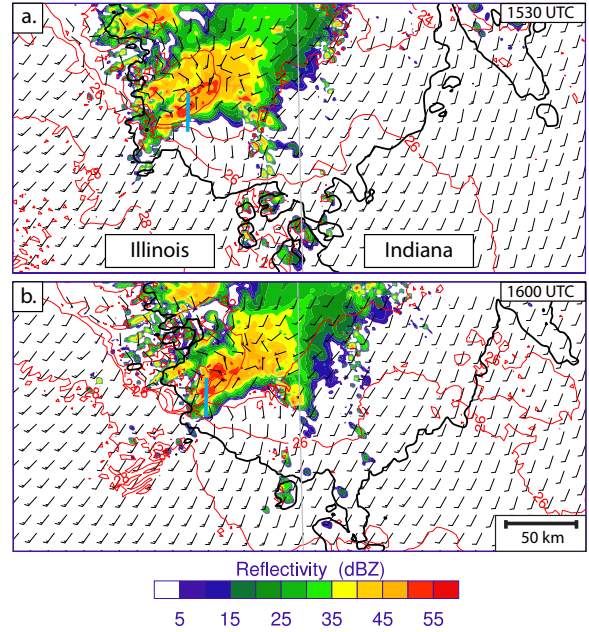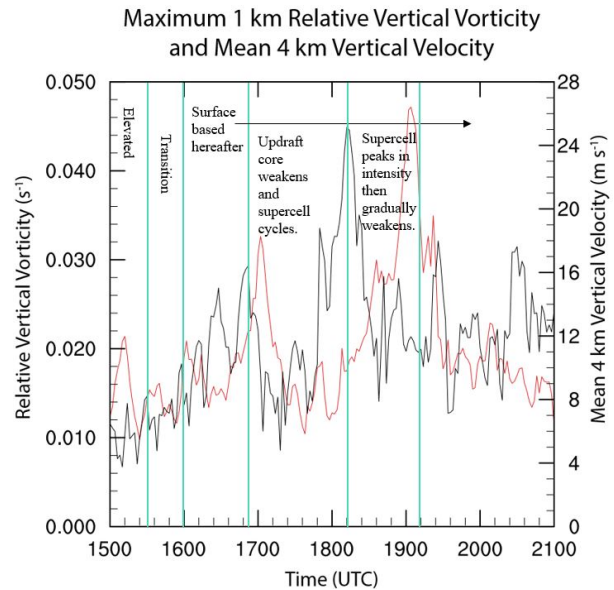

FIG. 6. Annotated time series of maximum 1 km ζ (red) and mean 4 km w (black) calculated over a 5×5 km grid centered on the maximum 1 km ζ.
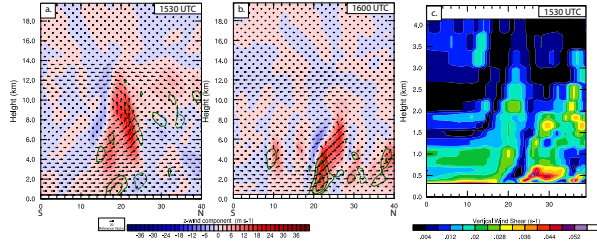
FIG. 7. South-to-north vertical cross sections of vertical velocity (m s^{-1}; shaded), vertical vorticity (s^{-1}; green; positive values solid and negative values dashed) contoured every 0.005 s^{-1}, and plane-parallel wind vectors (m s^{-1}; arrows) at (a) 1530 and (b) 1600 UTC. (c) Vertical wind shear (s^{-1}) in the surface to 4 km layer in the plane of the vertical cross section in (a). Units on the axes are km.
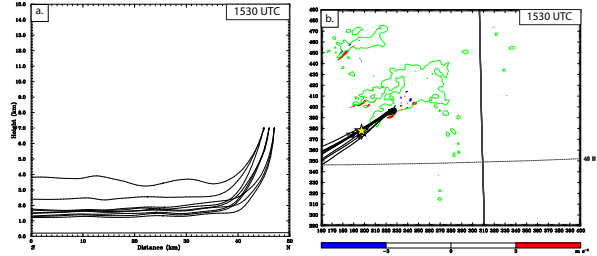

FIG. 8. (a) South-to-north vertical projection of the nine back trajectories centered on the strongest updraft at 1530 UTC. (b) A horizontal projection of the nine back trajectories, the 40 dBz simulated reflectivity contour at 1 km (green), and 1 km w ($>$ 3 m s^{-1} red and $<$-3 m s^{-1} blue). The star in (b) is the location of the model sounding in Fig. 9a taken at 1510 UTC when the parcels were near that location.

continues to be surface-based.

c. Trajectory analysis

Back trajectories were utilized to investigate from what level parcels within the maximum updraft originate between 1530-1600 UTC, when the convection becomes surface-based. A 3×3 grid of trajectories, each 1 km apart, was initialized within the maximum updraft and then integrated backward in time to 1400 UTC. Figure 8a demonstrates the the updraft indeed was elevated at 1530 UTC as all of the trajectories originate above 1 km. In a horizontal plan view of the trajectories (Fig.8b), all of the trajectories originate from the same area, indicating little vertical wind shear within the storm inflow layer. A model sounding was taken at the starred location in Fig. 8b and is displayed in Fig. 9a. Although the analyzed level of free convection (LFC) for an undilute surface parcel is around 900 mb, such a parcel does not become significantly buoyant until around 850 mb (blue arrow in Fig. 9a), owing to a moist-adiabatic layer below 850 mb. This is consistent with inflow parcels originating from just above 1 km above ground level (AGL) at this time (Fig. 8a).

As time progresses, trajectories from below 1 km begin to enter the updraft (Figs. 10a-c), such that the updraft is almost entirely ingesting near-surface air by 1558 UTC (Fig. 10d). The horizontal plan view of the trajectories within the maximum updraft at 1550 UTC indicates that trajectories originate from different horizontal locations, a manifestation of vertical wind shear in the storm inflow layer (Fig. 10e). The sounding from the starred location in Fig. 10e is displayed in Fig. 9b and exhibits some CAPE within the moist-adiabatic layer owing to surface heating, and is more supportive of air from be-
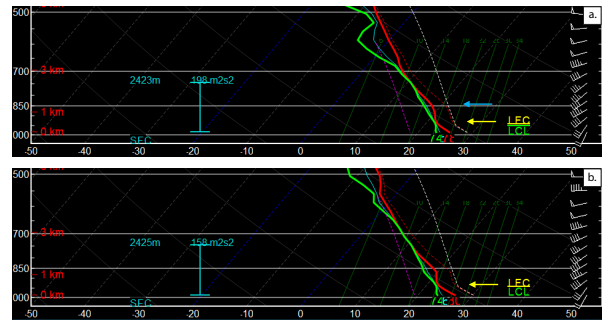

FIG. 9. Model soundings taken at (a) 1510 UTC from the location indicated in Fig. 8b and (b) 1530 UTC from the location indicated in Fig. 10e. The dashed white line is the most unstable parcel process curve and the dashed red curve is the environmental virtual temperature. Yellow arrows indicate the LFC. The blue arrow in (a) indicates the top of the moist adiabatic layer where a surface parcel becomes significantly buoyant.

low 1 km entering the updraft.

d. Vorticity budget analysis

Leading up to 1600 UTC in the simulation, there is an area of large 0-1 km storm-relative helicity (SRH; $>$ 400 m^2 s^{-2}) ahead of the storms underneath the anvil (Fig. 11a). SRH can become large through an increase in storm-relative winds, an increase in horizontal vorticity, or by the storm-relative wind and horizontal vorticity vectors becoming more parallel. Figure 11b demonstrates that all three of these are occurring beneath the
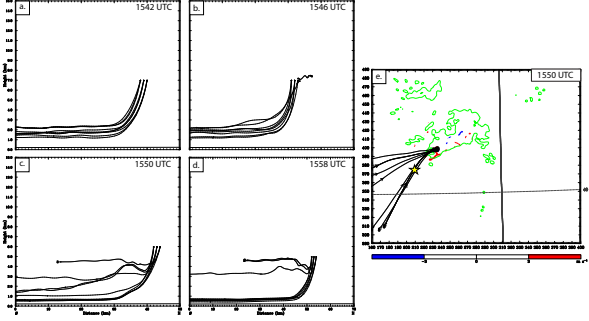
FIG. 10. As in Fig. 8a but for trajectories centered on the strongest updraft at (a) 1542, (b) 1546, (c) 1550, and (d) 1558 UTC. (e) As in Fig. 8b, but for the nine back trajectories in (c) and the star is the location of the model sounding taken at 1530 UTC in Fig. 9b.

anvil. Shaded in Fig. 11b is turbulent kinetic energy (TKE). Lower values of TKE exist underneath the anvil, where there is less vertical mixing, and higher values exist in the full sun, where vertical mixing is stronger. Since vertical mixing destroys vertical wind shear and thus horizontal vorticity, this is consistent with lower values of horizontal vorticity outside of the anvil cover.

We completed a vorticity budget analysis along trajectories that enter the 1 km updraft at 1600 UTC. The equations for the x and y components of horizontal vorticity are

$$\xi(t) = \xi_0 + \int_{t_0}^t \left(\eta \frac{\partial u}{\partial y} + \zeta \frac{\partial u}{\partial z} + \xi \frac{\partial u}{\partial x} + \frac{\partial B}{\partial y} \right) dt \quad (1)$$

$$\eta(t) = \eta_0 + \int_{t_0}^t \left(\xi \frac{\partial v}{\partial x} + \zeta \frac{\partial v}{\partial z} + \eta \frac{\partial v}{\partial y} - \frac{\partial B}{\partial x} \right) dt \quad (2)$$

where ξ is the x-component of horizontal vorticity and η is the y-component of horizontal vorticity. The first two terms inside the integral in each equation are the tilting terms, the third is the stretching term, and the last is the baroclinic generation term (e.g., Marquis et al. 2016). We calculated a residual for each component by subtracting the total calculated vorticity from the model output vorticity. The residual is assumed to represent frictional generation or dissipation of vorticity as well as subgrid-scale turbulent processes (i.e., vertical mixing).

Time series of each of the terms in (1) and (2) and the residuals are provided for select trajectories in Fig. 12. For most of the trajectories, the residuals generally increase in magnitude before the trajectories pass underneath the anvil. Afterward, the residuals remain relatively constant or decrease, meaning that the processes that led to an increase in the residuals either stopped or reversed. Outside of the anvil, the x-residuals become increasingly positive and the y-residuals become increas-
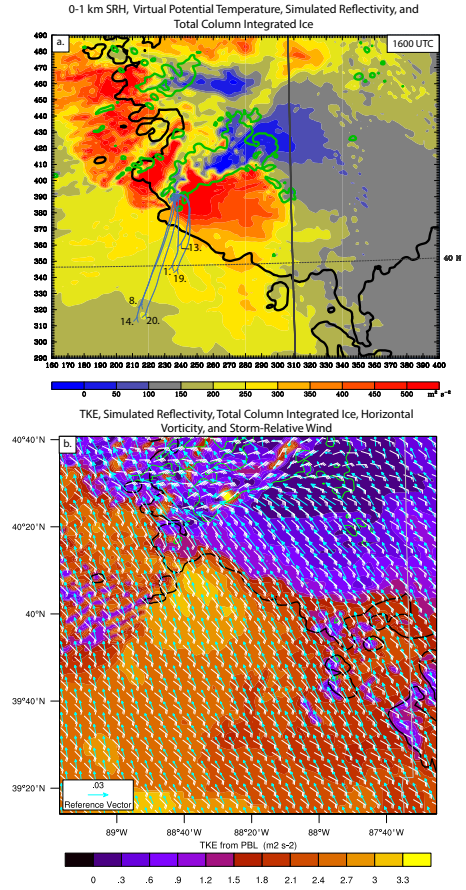

FIG. 11. (a) 0-1 km SRH (m^2 s^{-2}; shaded), 1 km simulated reflectivity (40 dBz; green), and total column integrated ice (0.1 kg m^{-2}; black) at 1600 UTC. Thin blue lines and arrows are select trajectories bound for the 1 km above mean sea level (MSL) updraft at 1600 UTC. (b) TKE at 25 m AGL (m^2 s^{-2}; shaded), 1 km simulated reflectivity (40 dBz; green), total column integrated ice (0.1 kg m^{-2}; black), horizontal vorticity at 550 m MSL (s^{-1}; blue arrows), and storm-relative winds at 550 m MSL (kts; white barbs) at 1540 UTC.

ingly negative, generating a horizontal vorticity vector directed toward the southeast. Figure 11b indicates that the ambient horizontal vorticity vector is oriented toward the northwest, meaning that the processes represented by the residuals are destroying the ambient horizontal vorticity. We believe that turbulent mixing is the reason for the decreased horizontal vorticity in the full sun, consistent with increased TKE, and lower 0-1 km SRH values. Furthermore, trajectory 13 (Fig. 12c) begins underneath the anvil and the residual pattern discussed above is not evident on this time series, lending more confidence that vertical mixing decreases the horizontal vorticity outside
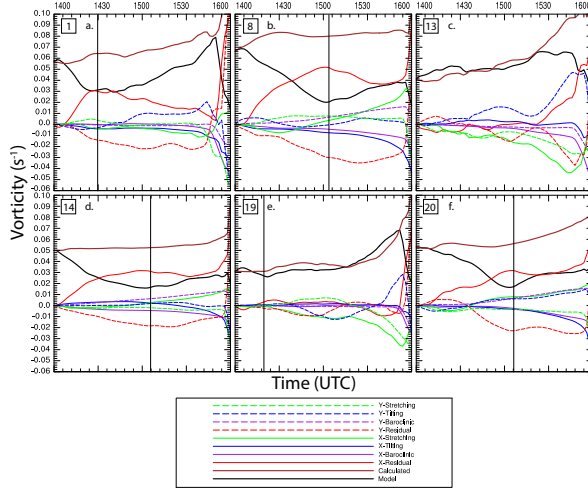
FIG. 12. Vorticity budgets of *x*-components (solid) and *y*-components (dashed) of stretching (green), tilting (blue), and baroclinic generation (purple) of horizontal vorticity for labeled trajectories in Fig. 11a. The sum of stretching, tilting, and baroclinic generation is given by the brown lines, and the model output horizontal vorticity is given by the black lines. The residual (red) is the calculated horizontal vorticity subtracted from the model output horizontal vorticity. Trajectories displayed are (a) 1, (b) 8, (c) 13, (d) 14, (e) 19, and (f) 20. Vertical black lines indicate when each trajectory enters underneath the anvil (missing in (c) because trajectory 13 begins underneath the anvil).

of the anvil cover. Trajectory 19 (Fig. 12e) exhibits a similar pattern; it only spends a short time outside of anvil cover. This analysis is consistent with that of Frame and Markowski (2010, 2013) who noted modulations in low-level shear beneath the anvils of simulated supercell thunderstorms.

e. Perturbation pressure decomposition

WRF output was interpolated to flat levels such that a perturbation pressure decomposition could be completed. The pressure diagnostic equation (e.g., Rotunno and Klemp 1982; Klemp and Rotunno 1983) is

$$\nabla^2 p' = -e_{ij}'^2 + \frac{1}{2}|\vec{\omega}'|^2 - 2\vec{S}\cdot\nabla_h w' + \frac{\partial B}{\partial z} \quad (3)$$

In this equation, p' is the perturbation pressure, e_{ij}' is the perturbation deformation tensor, $\vec{\omega}'$ is the vorticity vector of the perturbation flow, $\vec{S}$ is the environmental vertical wind shear vector, w' is the perturbation vertical velocity, and B is buoyancy. The first two terms on the right side of this equation are the non-linear dynamic terms. The

first of these is the contribution from deformation, meaning that convergence is associated with positive pressure perturbations. The second non-linear term is the contribution from rotation, in which rotation of either sign on the storm scale results in negative pressure perturbations. The third term is the linear dynamic term, yielding negative pressure perturbations downshear of updrafts and positive pressure perturbations upshear. The last term is the pressure contribution from buoyancy arising from density differences (e.g., Doswell and Markowski 2004). Negative buoyancy perturbation pressures generally occur where buoyancy increases with height and vice versa for positive perturbations (e.g., Warren et al. 2017). To investigate the vertical accelerations that result from these pressure perturbations, it is useful to examine the vertical derivative of (3) given by

$$\nabla^2 \frac{\partial p'}{\partial z} = -\frac{\partial}{\partial z}e_{ij}'^2 + \frac{1}{2}\frac{\partial}{\partial z}|\vec{\omega}'|^2 - 2\frac{\partial}{\partial z}(\vec{S}\cdot\nabla_h w') + \frac{\partial^2 B}{\partial z^2} \quad (4)$$

Hereafter, we abbreviate the vertical acceleration owing to the non-linear dynamic terms APDN, the acceleration owing to the linear dynamic term APDL, and the acceleration owing to the buoyancy term APB .

To calculate pressure perturbations, a base state is required. Since this WRF simulation was initialized with an inhomogeneous environment, a sensitivity test was conducted for various base state locations south, southwest, and west of the storm and averaged over an 11×11 km box (not shown). The mean and standard deviation of 10 base state profiles are provided in Fig. 13. The mean APDN indicates that it is the dominant acceleration at 1.5 km (compare Figs. 13a,c,e). The standard deviation of both APB and APDN are an order of magnitude smaller than the mean accelerations (Figs. 13a,b,e,f), indicating little variability owing to changing the base state. The standard deviation for APDL is relatively large, indicating a sensitivity to the base state location (Figs 13c,d). But since APDL is roughly an order of magnitude smaller than APDN at 1.5 km, any such sensitivity is relatively unimportant to this analysis. Having conducted our sensitivity test, we used a base state in the inflow 95 km south-southwest of the storm for the perturbation pressure decomposition. This location was checked at each time to make sure it was free of convection and precipitation.

Figure 14 depicts APDN at 900 m at times leading up to 1600 UTC. Positive values of 900 m APDN are generally co-located with rotation of either sign at 2 km (green and pink contours in Fig. 14). Vertical cross sections were taken through an area of positive APDN where an updraft develops during this period (blue lines and black contour in Fig. 14). The north-south and east-west vertical cross sections at 1546 UTC display an elevated updraft with ζ on the order of 0.01 s^{-1} (Fig. 15). Below this
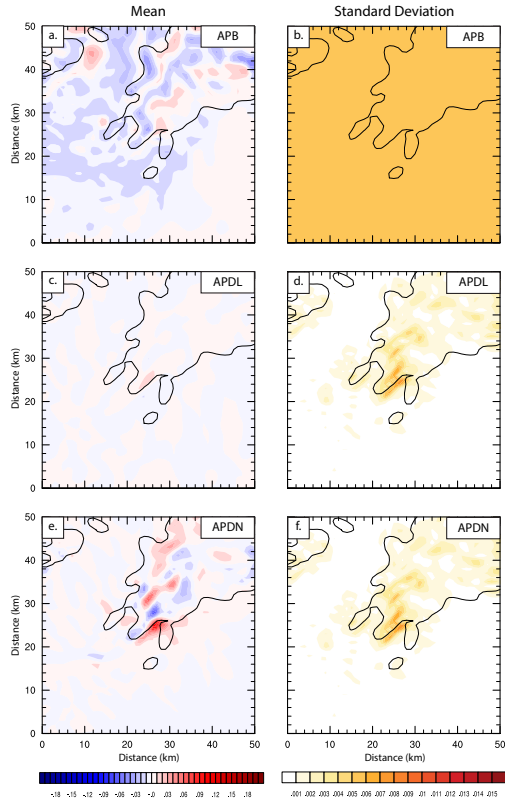
FIG. 13. The mean (a) APB, (c) APDL, and (e) APDN ($m\ s^{-2}$; shaded) and standard deviation ($m\ s^{-2}$; shaded) of (b) APB, (d) APDL, and (f) APDN at 1.5 km produced from the sample of ten base-state locations. The 40 dBZ simulated reflectivity contour at 1 km is in black. All plots are at 1600 UTC.

FIG. 14. APDN at 900 m ($m\ s^{-2}$; shaded), vertical velocity at 1 km (contoured every 5 $m\ s^{-1}$; black), vertical vorticity at 2 km (contoured every 0.005 s^{-1}; positive values in green, negative values in pink, and zero contour suppressed for clarity), and 40 dBZ simulated reflectivity contour at 1 km (thin dark green line) at (a) 1546, (b) 1550, (c) 1556, and (d) 1600 UTC. Blue lines in (a) and (d) are the locations of the vertical cross sections in Figs. 15 and 16.

elevated updraft and vortex is a column of upward APDN on the order of 0.03 $m\ s^{-2}$ over a depth of roughly 5 km.

Over time, the elevated updraft builds downward toward the surface. As near-surface air is ingested, the horizontal vorticity generated by the 0-1 km vertical wind shear is tilted and ζ of 0.015 s^{-1} develops below 1 km by 1600 UTC (Fig. 16). As ζ increases near the surface, downward APDN develops in the upper portion of the updraft owing to rotation decreasing with height (Figs. 16a,b). Despite the downward acceleration, the updraft grows and intensifies after this time. Upward APB likely offsets much of the downward APDN in the upper portions of the updraft (compare the locations of downward APDN in Figs. 16a,b with upward APB in Figs. 16c,d).
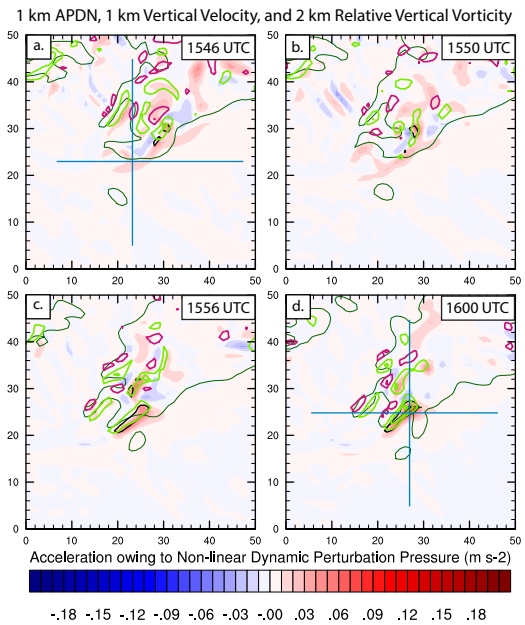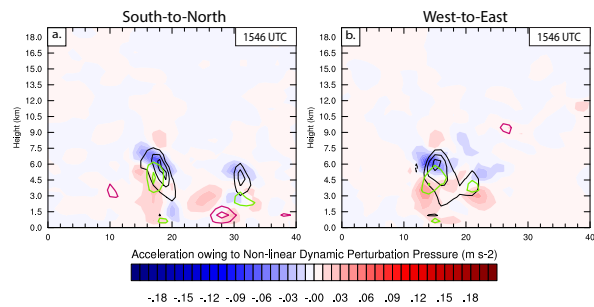

FIG. 15. Vertical cross sections of APDN ($m\ s^{-2}$; shaded), vertical velocity (contoured every 5 $m\ s^{-1}$; black), and vertical vorticity (contoured every 0.005 s^{-1}; positive values in green, negative values in pink, and zero contour suppressed for clarity) along the blue lines in Fig. 14a at 1546 UTC.
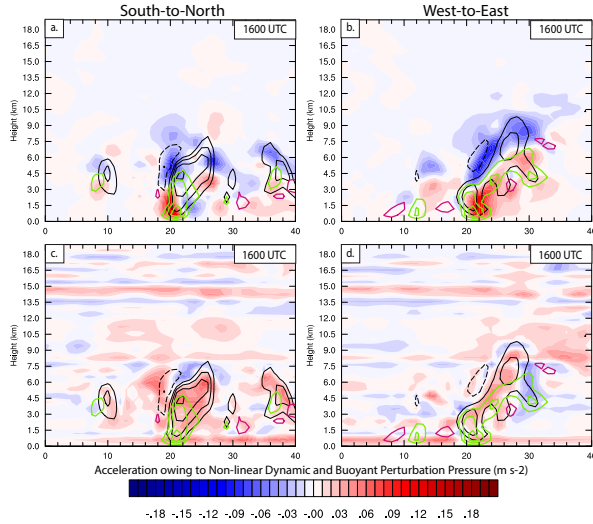
FIG. 16. (a,b) As in Fig. 15a,b but along the lines in Fig. 14d at 1600 UTC. (c,d) As in (a,b) but APB is shaded.

4. Conclusions

A surprise tornado outbreak with 24 confirmed tornadoes impacted Indiana and Ohio on 24 August 2016 and six of these tornadoes were significant. Elevated and unorganized storms formed along an outflow boundary owing to convection the prior evening while an MCV tracked across northern Illinois and Indiana. Convection ahead of the main cluster created a differential heating boundary that progressed northward during the outbreak. As storms entered Indiana, the cluster developed into three discrete surface-based supercells, each of which produced significant tornadoes that coincided with the location of this boundary.

A WRF simulation captures the MCV, differential heating boundary, and storm mode transition. Vertical cross sections through the first developing supercell suggest that the storm becomes surface based between 1530-1600 UTC. This is confirmed by a trajectory analysis as trajectories within the maximum updraft originate from near the surface by 1600 UTC. Model soundings indicate a moist-adiabatic layer from 900-850 mb and continued surface heating allows for some CAPE to develop in this layer, permitting surface air to be ingested by the updrafts.

Vorticity budgets for trajectories entering the 1 km updraft at 1600 UTC indicate that horizontal vorticity is decreased by vertical mixing outside of the anvil cover. The vertical mixing destroys vertical wind shear and thus horizontal vorticity, consistent with higher values of TKE, lower horizontal vorticity magnitudes, and lower 0-1 km

SRH outside of the anvil cover. Trajectories that begin underneath or close to the anvil edge do not exhibit the same decrease in horizontal vorticity owing to vertical mixing. Once trajectories pass under the anvil cover, horizontal vorticity is generally preserved. This lends confidence that the observed differential heating boundary in Indiana was a crucial feature in the development of supercells and tornadoes on 24 August. With less mixing north of the differential heating boundary, 0-1 km SRH was preserved and ingested by the updrafts as they became surface based, providing rotation necessary for supercell development.

A perturbation pressure decomposition indicates that modest rotation within elevated updrafts induced upward-directed APDN over a depth of roughly 5 km. This acceleration may have aided parcels in rising through the moist adiabatic layer found on model soundings, promoting the transition from elevated to surface-based convection. As surface-based updrafts develop, horizontal vorticity near the surface is tilted and stronger ζ develops near the surface, driving an upward APDN at the surface, aiding in low-level updraft intensification. A downward APDN develops aloft within the updraft. This downward APDN may be offset by upward APB in the same location in this case. The offsetting accelerations may allow updrafts to persist when near-surface ζ becomes strong.

An important takeaway from this event is that environments favorable for supercells and tornadoes should not necessarily be discounted if convection-allowing models do not depict cellular convection. Improved model data assimilation or microphysical parameterizations may mitigate this issue in the future. The analysis of observations and identification of boundaries is also crucial for a qualitative understanding of the mesoscale environment. Despite a challenging forecast, we are thankful to the operational and broadcast meteorologists who delivered warnings to the public during this event. Their efforts prevented any fatalities and are commended.

REFERENCES

Bluestein, H. B., and M. L. Weisman, 2000: The interaction of numerically simulated supercells initiated along lines. *Mon. Wea. Rev.,* **128**, 3128-3149.

Burgess, D. W., and E. B. Curran, 1985: The relationship of storm type to environment in Oklahoma on 26 April 1984. *Preprints, 14th Conf. on Severe Local Storms,* Indianapolis IN, Amer. Meteor. Soc., 208-211.

Clark, A. J., J. Gao, P. Marsh, T. Smith, J. Kain, J. Correia, M. Xue, and F. Kong, 2013: Tornado pathlength forecasts from 2010 to 2011 using ensemble updraft helicity. *Wea. Forecasting,* **28**, 387-407.

Doswell, C. A., III, and P. M. Markowski, 2004: Is buoyancy a relative quantity? *Mon. Wea. Rev.,* **132**, 853-863.

Finley, C. A., W. R. Cotton, and R. A. Pielke, Sr., 2001: Numerical simulation of tornadogenesis in a high-precipitation supercell. Part I: Storm evolution and transition into a bow echo. *J. Atmos. Sci.,* **58**, 1597-1629.

Frame, J. W., and K. T. Gray, 2018: A mesoscale analysis of the development of storms and transition to supercells during the Indiana and Ohio tornado outbreak of 24 August 2016. *29th Conf. on Severe Local Storms,* Stowe, VT, Amer. Meteor. Soc.

Frame, J. W., and P. M. Markowski, 2010: Numerical simulations of radiative cooling beneath the anvils of supercell thunderstorms. *Mon. Wea. Rev.,* **138**, 3024-3047.

Frame, J. W., and P. M. Markowski, 2013: Dynamical influences of anvil shading on simulated supercell thunderstorms. *Mon. Wea. Rev.,* **141**, 2802-2820.

Geerts, B., and Coauthors, 2017: The 2015 Plains Elevated Convection at Night field project. *Bull. Amer. Meteor. Soc.,* **98**, 767-786.

Iacono, M. J., E. J. Mlawer, S. A. Clough, and J.-J. Morcrette, 2000: Impact of an improved longwave radiation model, RRTM, on the energy budget and thermodynamic properties of the NCAR Community Climate Model, CCM3. *J. Geophys. Res.,* **105**, 14873-14890.

Jiménez, P. A., J. Dudhia, J. F. González-Rouco, J. Navarro, J. P. Montávez, and E. García-Bustamante, 2012: A revised scheme for the WRF surface layer formulation. *Mon. Wea. Rev.,* **140**, 898-918.

Klemp, J. B., and R. Rotunno, 1983: A study of the tornadic region within a supercell thunderstorm. *J. Atmos. Sci.,* **40**, 359-377.

Livneh, B., P. J. Restrepo, and D. P. Lettenmaier, 2011: Development of a unified land model for prediction of surface hydrology and landatmosphere interactions. *J. Hydrometeor.,* **12**, 1299-1320.

Marquis, J. N., Y. P. Richardson, P. Markowski, D. Dowell, J. Wurman, and K. Kosiba, 2016: An investigation of the Goshen County, Wyoming, tornadic supercell of 5 June 2009 using EnKF assimilation of mobile mesonet and radar observations collected during VORTEX2. Part II: Mesocyclone-scale processes affecting tornado formation, maintenance, and decay. *Mon. Wea. Rev.,* **144**, 3441-3463, https://doi.org/10.1175/MWR-D-15-0411.1.

Milbrandt, J. A., and M. K. Yau, 2005: A multimoment bulk microphysics parameterization. Part I: Analysis of the role of the spectral shape parameter. *J. Atmos. Sci.,* **62**, 3051-3064.

Mlawer, E. J., S. J. Taubman, P. D. Brown, M. J. Iacono, and S. A. Clough, 1997: Radiative transfer for inhomogeneous atmospheres: RRTM, a validated correlated-k model for the longwave. *J. Geophys. Res.,* **102**, 16663-16682.

Nakanishi, M., and H. Niino, 2006: An improved Mellor-Yamada level-3 model: Its numerical stability and application to a regional prediction of advection fog. *Bound.-Layer Meteor.,* **119**, 397-407.

Parker, M. D., 2008: Response of simulated squall lines to low-level cooling. *J. Atmos. Sci.,* **65**, 1323-1341.

Rotunno, R., and J. B. Klemp, 1982: The influence of the shear-induced pressure gradient on thunderstorm motion. *Mon. Wea. Rev.,* **110**, 136-151.

Skamarock, W. C., and Coauthors, 2008: *A Description of the Advanced Research WRF Version 3.* NCAR Technical Note NCAR/TN-475+STR, doi:10.5065/D68S4MVH.

Xue, M., K. K. Droegemeier, and V. Wong, 2000: The Advanced Regional Prediction System (ARPS): A multi-scale nonhydrostatic atmospheric simulation and prediction model. Part I: Model dynamics and verification. *Meteor. Atmos. Phys.,* **75**, 161-193.